

VERA and ALMA Observations of the H₂O Supermaser Burst in Orion KL

Tomoya HIROTA^{1,2} Masato TSUBOI³ Yasutaka KURONO^{4,5} Kenta FUJISAWA^{6,7} Mareki HONMA^{1,2} Mi Kyoung KIM⁸ Hiroshi IMAI⁹ and Yoshinori YONEKURA¹⁰

¹*National Astronomical Observatory of Japan, Mitaka, Tokyo 181-8588*

²*Department of Astronomical Sciences, The Graduate University for Advanced Studies (SOKENDAI), Mitaka, Tokyo 181-8588*

tomoya.hirota@nao.ac.jp

³*Institute of Space and Astronautical Science, Japan Aerospace Exploration Agency, Sagami-hara, Kanagawa 229-8510*

⁴*Chile Observatory, National Astronomical Observatory of Japan, Osawa 2-21-1, Mitaka, Tokyo 181-8588*

⁵*Joint ALMA Observatory, Alonso de Cordova 3107 Vitacura, Santiago 763-0355, Chile*

⁶*Department of Physics, Faculty of Science, Yamaguchi University, Yamaguchi, Yamaguchi 753-8512*

⁷*The Research Institute of Time Studies, Yamaguchi University, Yamaguchi, Yamaguchi 753-8511*

⁸*Korea Astronomy and Space Science Institute, Hwaam-dong 61-1, Yuseong-gu, Daejeon, 305-348, Republic of Korea*

⁹*Graduate School of Science and Engineering, Kagoshima University, Kagoshima, Kagoshima 890-0065*

¹⁰*Center for Astronomy, Ibaraki University, Mito, Ibaraki 310-8512*

(Received ; accepted)

Abstract

The 22 GHz H₂O maser in Orion KL has shown extraordinary burst events in 1979-1985 and 1998-1999, sometimes called supermaser. We have conducted monitoring observations of the supermaser in Orion KL using VERA, VLBI Exploration of Radio Astrometry, in the current third burst since 2011 March. Three flux maxima are detected in 2011 and 2012 with rising and falling timescales of 2-7 months. Time variations of the supermaser seem symmetric for all of the active phases. The maximum total flux density of 135000 Jy is observed in 2012 June while it is still one order of magnitude lower than those in previous bursts. The supermaser consists of two spatially different components at different velocities. They are elongated along a northwest-southeast direction perpendicular to the low-velocity outflow driven by Source I. Proper motions of the supermaser features with respect to Source I are measured toward west and southwest directions, almost parallel to the low-velocity

outflow. The flux density and linewidth show an anti-correlation as expected for an unsaturated maser emission. The supermaser is located close to the methylformate (HCOOCH_3) line and continuum emission peaks in the Orion Compact Ridge detected by ALMA, Atacama Large Millimeter/Submillimeter Array. The broader velocity range of the weak HCOOCH_3 emission at the supermaser position would be an evidence of a shock front. On the other hand, the 321 GHz H_2O line is not detected at the position of the supermaser. It can be explained qualitatively by one of the theoretical H_2O excitation models without extraordinary conditions. Our results support a scenario that the supermaser is excited in the dense gas interacting with the low-velocity outflow in the Compact Ridge. The extremely high flux density and its symmetric time variation for rising and falling phases could be explained by a beaming effect during the amplification process rather than changes in physical conditions.

Key words: ISM: individual objects (Orion KL) — ISM: molecules — masers — radio lines: ISM

1. Introduction

Orion KL (Kleinmann-Low object) is one of the nearest massive star-forming regions at a distance of 420 pc (Menten et al. 2007; Kim et al. 2008) and hence, has been the most extensively studied source in the context of star-formation study (Genzel & Stutzki 1989; Bally 2008). There are powerful outflows and jets possibly associated with young stellar objects (YSOs) in this region at a wide range of spatial scales from <100 AU to >10000 AU. They are traced by various molecular lines such as vibrationally excited SiO masers at 43 GHz (Kim et al. 2008; Matthews et al. 2010; Kim et al. 2014), 22 GHz H_2O maser (Genzel et al. 1981; Gaume et al. 1998; Hirota et al. 2007; Greenhill et al. 2013; Kim et al. 2014), millimeter/submillimeter thermal SiO (Plambeck et al. 2009; Zapata et al. 2012; Niederhofer et al. 2012) and CO lines (Beuther & Nissen 2008; Zapata et al. 2009), and near-infrared H_2 line (Allen & Burton 1993; Kaifu et al. 2000; Bally et al. 2011). These observational studies have revealed physical properties of the outflows, jets, and surrounding shocked materials interacting with ambient clouds.

Among a number of tracers, the 22 GHz H_2O maser is known to be a unique tracer to investigate a three-dimensional velocity structure. Thanks to its extremely high brightness, it can be detected by high-resolution interferometers and very long baseline interferometers (VLBI) providing a capability of proper motion measurements. As a result, the 22 GHz H_2O maser in Orion KL is found to be tracing a low-velocity outflow along a northeast-southwest axis (Genzel et al. 1981; Hirota et al. 2007; Greenhill et al. 2013; Kim et al. 2014) centered

at a strong radio continuum source labeled I (Churchwell et al. 1987; Menten & Reid 1995). Hereafter we call this Source I.

One of these H₂O maser features in Orion KL has exhibited an enormous outburst, which is sometimes called supermaser. The H₂O maser burst in Orion KL was reported in 1979-1985 for the first time (Matveenko et al. 1988; Garay et al. 1989) followed by 1998-1999 (Omodaka et al. 1999; Matveyenko et al. 2004; Shimoikura et al. 2005). Based on VLBI observations, the supermaser was revealed to have east-west or northwest-southeast elongations in 1979-1985 and 1998-1999, respectively. The line-of-sight velocity with respect to the local standard of rest (LSR) was stable at $\sim 8 \text{ km s}^{-1}$, suggesting a common origin. Although the maser burst could be related to star-formation activities in Orion KL, either a circumstellar disk (Matveenko et al. 1988; Shimoikura et al. 2005) or a jet/outflow driven by a YSO (Garay et al. 1989; Matveyenko et al. 2004), its origin and mechanism are still under debate.

The third burst of the H₂O maser in Orion KL has started since February 2011 (Tolmachev 2011; Otto & Gaylard 2012; Matveyenko et al. 2012a; Matveyenko et al. 2012b). The burst appears to be possibly periodic with an interval of about 13 years (1985, 1998, and 2011). It could support the hypothesis of a common origin (Tolmachev 2011). We have carried out astrometric monitoring observations with VLBI Exploration of Radio Astrometry (VERA) since 2011 March (Hirota et al. 2011) and studied basic properties of the supermaser. Main conclusions by Hirota et al. (2011) are (1) the burst occurs at two spatially nearby but distinct components (separation of $\sim 10 \text{ mas}$) at the LSR velocities of 6.95 and 7.58 km s^{-1} (hereafter we call them "6.9 km s^{-1} " and "7.5 km s^{-1} " features, respectively, using representative velocities) as reported in previous bursts (Matveenko et al. 1988; Garay et al. 1989; Omodaka et al. 1999; Matveyenko et al. 2004; Shimoikura et al. 2005), (2) these features are elongated along a northwest-southeast direction perpendicular to the low-velocity outflow and their proper motions are parallel to the outflow axis, and (3) the absolute position of the supermaser is coincident with a shocked molecular gas called the Orion Compact Ridge. All of these characteristics suggest that the supermaser could be excited in an interacting region between the low-velocity outflow and the ambient gas in the Compact Ridge (Genzel et al. 1981; Liu et al. 2002; Favre et al. 2011; Brouillet et al. 2013).

Nevertheless, the maximum flux density for the current burst phase is reported to be 44000 Jy on May 2011 (Hirota et al. 2011). It is much lower than those in previous bursts in which the flux densities of the supermaser reached 10^6 Jy (Matveenko et al. 1988; Garay et al. 1989; Omodaka et al. 1999; Matveyenko et al. 2004; Shimoikura et al. 2005). Although the maser bursts could have possible periodicity of 13 years, 1985, 1998, and 2011, it is still unclear whether all of three events are caused by a common origin. In order to understand their origin and to reveal their relationship between star-formation activities in Orion KL in relation to outflows, jets, and interaction with ambient clouds, it is important to continue further monitoring observations of the supermaser at a current valuable opportunity.

In this paper, we report results of our continued monitoring observations of the supermaser with VERA to investigate time variations of their properties. In addition, we present follow-up observations with Atacama Large Millimeter/Submillimeter Array (ALMA) to identify possible powering source(s), as well as to study pumping mechanisms based on multi-transition H₂O lines. Although we find that the current burst activity is lower by a factor of 10 than those in previous bursts in terms of the maser flux density as discussed later, we call the current bursting maser feature "supermaser" throughout the present paper.

2. Observations

2.1. VERA

Observations of the $6_{1,6}-5_{2,3}$ transition of H₂O at 22.235080 GHz (Kukolich 1969; Chen et al. 2000) in Orion KL were carried out with VERA. Details of the observations have been described in separate papers (Hirota et al. 2007; Hirota et al. 2011), and we briefly summarize key parameters in this section. VLBI monitoring observations have been conducted regularly since 2011 March with a typical interval of 1-4 weeks. The maximum baseline length of VERA is 2270 km and the resultant fringe-spacing is 1.2 mas. We employed the dual beam observation mode, in which Orion KL and an ICRF source J054138.0-054149 (Ma et al. 1998) were observed simultaneously, to measure the absolute position of the target H₂O maser in Orion KL with respect to the positional reference source. The astrometric accuracy is estimated to be 0.4 mas according to post-fit residuals of proper motion measurements. These two sources were observed for 8 hours being tracked from horizon to horizon at the lowest elevation angle of ~ 15 degrees. A typical on-source time was 6 hours for each epoch. In this paper, we report the astrometric and imaging results of the first 18 epochs of observations from 2011/068 to 2012/269 (hereafter we indicate an epoch of observation as year/day of the year). A spectral resolution was set to be 15.625 kHz, corresponding to a velocity resolution of 0.21 km s⁻¹. Calibration and synthesis imaging were performed using the NRAO Astronomical Image Processing System (AIPS) software package in the same manner employed previously (Hirota et al. 2007; Hirota et al. 2011).

We also used other data of VERA observations at 22 GHz including Orion KL as a fringe-finder to investigate a time variation in spectral profiles. A total number of spectral line monitoring data is 53 epochs from 2008/329 to 2014/025. On-source integration times of each spectral line monitoring data for Orion KL was 5-10 minutes.

2.2. ALMA

In addition, we used ALMA data taken in one of the early science projects in cycle 0 (ADS/JAO.ALMA#2011.0.00199.S) to compare images of submillimeter continuum emissions and molecular lines. Observations were carried out at the ALMA band 7 (in the range of 320-340 GHz) on 2012 July 16, August 25, and October 21. They were almost coincident with the

most active burst phase as discussed in the next section. In this paper, we mainly focus on the $10_{2,9}-9_{3,6}$ H_2O line at 321.225656 GHz (Chen et al. 2000) and methyl formate (HCOOCH_3) lines close to the H_2O line. The maximum baseline length in our ALMA observations was 400 m, corresponding to a spatial resolution of $\sim 0.5''$, depending on the UV weighting in the imaging. Synthesis imaging and self-calibration were done with the Common Astronomy Software Applications (CASA) package. Further details of observations are reported elsewhere (Hirota et al. 2014a; Hirota et al. 2014b).

3. Results

3.1. Time variation of the 22 GHz H_2O maser

Figure 1 shows spectra of the supermaser observed in 18 epochs of the regular astrometry observations from 2011 to 2012, and Figure 2 shows time variations of the flux density, velocity width, and peak velocity for all the observed epochs including both 18 epochs of the regular astrometry and 53 epochs of the spectral line monitoring observations. First, these parameters are determined by fitting a single Gaussian to the observed profile. However, there are two distinct velocity components at $\sim 6.9 \text{ km s}^{-1}$ and $\sim 7.5 \text{ km s}^{-1}$ as reported in Hirota et al. (2011). These components can be clearly seen in spectral profiles such as the double-peaked structure on 2011/121 and 2011/137 and red-shifted shoulder on 2011/208 (Figure 1). This results in a significant deviation from the observed line profile in the fitting. Thus, we next fit two Gaussians to the observed profiles for these epochs. Although these line parameters show slightly larger error bars as shown in Figure 2, we can see time variations of flux density, velocity width, and peak velocity for the $\sim 7.5 \text{ km s}^{-1}$ component continuously changing even during this phase. In contrast, the velocity component that appeared later at $\sim 6.9 \text{ km s}^{-1}$ shows a different time variation.

According to characteristics of the time variation in Figure 2, we can divide the monitoring period of the current H_2O maser burst into four phases; a moderately active phase in 2009 followed by a relatively quiescent phase in 2010, a start of the burst with rapid variation in 2011, the maximum phase in 2012, and a quiescent/possible initial phase of the next burst in 2013.

In 2009, there is a moderately active phase slowly increasing and decreasing in the flux density both in total power and cross power spectra. Timescales of both rising and falling phases, which are defined as periods from minimum to maximum and maximum to minimum flux densities, respectively, are almost equal, 10 months and 11 months, respectively (Figure 3(a)). During this phase, the peak velocity is also slightly changing from 7.4 to 7.3 km s^{-1} while the velocity width, $\sim 0.8 \text{ km s}^{-1}$, is almost stable with time. After this moderately active phase in 2009, the maser activity becomes a quiescent phase, whereas the total and correlated flux densities are as high as 2400 Jy and 500 Jy, respectively, at the minimum phase on 2010/227.

Toward this minimum phase, the velocity width of the total-power spectrum gradually increases although that of the cross-power spectrum shows a decreasing trend. At the minimum phase on 2010/227, the velocity width and peak velocity change drastically. Furthermore, these parameters show significant differences between total-power and cross-power spectra but with larger uncertainties than other epochs. This could be caused by other velocity components as their contributions become more and more significant relative to that of the 7.5 km s^{-1} component. Before and after this minimum phase, there were breaks of monitoring observations each for 100 days due to the maintenance of the VERA antennas, and hence, we could not trace time variations in this quiescent phase.

The H_2O maser burst has started in the end of 2010 or the beginning of 2011 (Tolmachev 2011). The flux density of the total-power spectrum at $\sim 7.5 \text{ km s}^{-1}$ has started to increase since 2010/350 while that of the cross power spectrum is temporarily halted on 2010/360 followed by the brightening from 2011/023. Although there is a lack of maser images, this might reflect a variation in the spatial structure of the emitting region. At the beginning of the current burst phase in 2011, there are two maximum phases on 2011/60-2011/121 and 2011/296-2011/311 with the total flux density of about 50000 Jy (Figure 2). The timescales of rising and falling phases are 7 months and 3 months, respectively, for the maximum phase of 2011/60-2011/121 (Figure 3(b)), although the flux density in this phase shows a variability rather than a monotonic increase or decrease. The timescales for the subsequent maximum phase of 2011/296-2011/311 (Figure 3(c)) are 2 months for both rising and falling phases. Apart from the different timescales, the behaviors in rising and falling phases seem to be symmetric as seen in the active phase in 2009 (Figure 3). As discussed above, the burst appears to occur in two different velocity components at 6.9 km s^{-1} and 7.5 km s^{-1} (Hirota et al. 2011) as seen in Figures 2(b) and (c).

The burst activity is temporarily stopped at the end of 2011, but more active burst has started in early 2012. The maximum total flux density of 135000 Jy is recorded on 2012/154 at the peak velocity of 7.4 km s^{-1} . In this most active phase, the flux density monotonically increases with the timescale of 5 months. The velocity width is about $0.60\text{-}0.75 \text{ km s}^{-1}$, which is the narrowest value observed in our monitoring as shown in Figure 2(b). On 2012/123, the derived velocity widths show the minimum values of $0.50 \pm 0.02 \text{ km s}^{-1}$ and $0.46 \pm 0.02 \text{ km s}^{-1}$ for the total-power and cross-power spectra, respectively. Only in this epoch, the velocity widths are significantly narrower than those observed just before and after this epoch (2012/107 and 2012/145). Due to the lack of maser images on 2012/123, we do not discuss what is the true reason for these narrower velocity widths only at this epoch. The flux density of the maser decreases with the timescale of 4 months after this maximum phase. It should be noted that the time variations in rising and falling phases again seem to be symmetric as seen in Figure 3(d). At the end of the burst phase in 2012/265 and 2012/269, the peak velocities of cross-power spectra show significant differences from those of the total-power spectra. They are thought

to be the results of significant contributions from other velocity components and/or effects of structure changes in maser features. This effect is seen particularly in less active phases such as in 2010.

Finally, the burst activity seems to end around 2012/269 while it again appears to be brightening from 2013/138. It is most likely an ignition of a newly occurred burst event. We will continue monitoring observations with VERA of the time variation of the supermaser in Orion KL. Still, the activity of the 22 GHz H₂O maser burst in 2011-2012 is relatively lower by a factor of 10 in comparison with the previous bursts in which the peak flux densities reached 10⁶ Jy.

We note that the fluxes reported in Figures 2 and 3 are those integrated over the whole region including both the supermaser and other features. We investigate possible contribution from other maser features at almost the same velocity with the supermaser feature in the 18 epochs of our VLBI imaging. Although it is difficult to make full channel maps with a wide field of view of an order of 10'', we search for positions of the maser features detected by Gaume et al. (1998). As a result, we detect one maser feature around the position offset of ($\sim 3.175''$, $\sim -1.850''$) in right ascension and declination, respectively, with respect to the supermaser feature. Gaume et al. (1998) detected two maser features near this position at the velocities of 6.3 km s⁻¹ and 7.6 km s⁻¹ with the flux densities of 21.0 Jy and 897.7 Jy, respectively. Figure 4 shows the flux density of this maser feature (we call this feature "SE feature") and the flux density ratio relative to the supermaser feature. The flux density of the SE feature increases with time and the maximum phase is observed on 2012/244. It is about 2 months after the maximum phase of the supermaser. Even around the maximum phase of the SE feature, a possible contribution to the total flux density is as large as 8% as shown in Figure 4 (b). Therefore, we conclude that the contamination from other maser features including the SE features are not significant in Figures 2 and 3.

3.2. Relationship between the linewidth and flux density

The time variation of the linewidth of the supermaser implies an anti-correlation with the flux density as shown in Figure 5. According to model calculations, the line profile of the maser first tends to be narrower as its intensity increases as long as the maser is unsaturated (Goldreich & Kwan 1974). Then the maser line starts to rebroaden when it becomes saturated (Goldreich & Kwan 1974). Under the condition of an unsaturated maser, the logarithm of the flux density of the maser line, $\log F$, is predicted to be proportional to the inverse square of the linewidth, Δv^{-2} . In Figure 5, we also show best-fit results;

$$\log F = A + B\Delta v^{-2}. \quad (1)$$

Our results may suggest that the supermaser in the current burst phase is still unsaturated. It is consistent with the observed narrow linewidths, 0.40-0.48 km s⁻¹, of the supermaser in 1998-1999 possibly attributed to the line narrowing for an unsaturated maser (Shimoikura

et al. 2005). In contrast, no clear relationship between the flux density and linewidth is found in the burst in 1979-1985 (Garay et al. 1989), suggesting a saturated maser emission. The difference in the degree of saturation could be attributed to the lower flux density, $\sim 10^5$ Jy in the current burst phase than those in the previous bursts, $>10^6$ Jy (Garay et al. 1989). We note that the line narrowing is predicted to occur even for a saturated maser if a stimulated emission rate is not large compared with the cross-relaxation rate (Goldreich & Kwan 1974). This means that the above relation holds when the maser flux density is not enough large regardless of saturated or unsaturated cases. Thus, we cannot firmly estimate the degree of saturation of the supermaser by judging from the linewidth-flux density relation only.

3.3. Maser maps and proper motion measurements

Figure 6 represents channel maps of the phase-referenced images of the supermaser in 2011/137. Three spatially distinct components are found in the initial phase of the burst from 2011/068 to 2011/137 as reported previously (Hirota et al. 2011). It is well known that the 22 GHz H_2O line ($6_{1,6}-5_{2,3}$) has a hyperfine structure with 3 main components and that the $F=7-6$ and $5-4$ components appear with the separation of $+0.45 \text{ km s}^{-1}$ and -0.58 km s^{-1} with respect to the central component, $F=6-5$ (Kukolich 1969). The velocity separation of -0.58 km s^{-1} is consistent with that observed for two bursting features. However, our results suggest that the two velocity components observed at 6.9 km s^{-1} and 7.5 km s^{-1} in the supermaser are not emitted from the same masing gas clump. Thus, these two velocity components are unlikely due to the hyperfine structure but they corresponds to distinct masing gas clumps with different positions and velocities.

We conduct two-dimensional Gaussian fittings on the phase-referenced images to measure the absolute position of each maser spot. Hereafter, we define a "spot" as a maser emission identified in a single velocity channel and a "feature" as a group of spots that are spatially coincident in two or more consecutive velocity channels. By using these results, we derive the absolute proper motions of the detected spots as summarized in Table 1 and Figure 7. We find that the northern feature, feature 1 (or spots 1, 3, and 5), is detectable only until 2011/296 (Table 1). The lifetime of the northern feature 1 is about 8 months. Given the typical monitoring interval and detection criterion, in which a spot is regarded as real when it is detected for more than three contiguous epochs, we might miss a short-term variation of a maser spot on phase-referenced images within a lifetime of less than ~ 2 months.

According to the absolute proper motion measurements, the supermaser features are apparently moving toward south and southwest directions as shown in the gray arrows in Figure 6. The derived proper motions are consistent but are more reliable than those previously obtained (Hirota et al. 2011) because we have continued the proper motion measurements in a longer observing period. When we subtract a modulation of an annual parallax of 2.39 mas (Kim et al. 2008) and the absolute proper motion of a possible powering source of the low-

velocity outflow, Source I ($\mu_\alpha \cos \delta, \mu_\delta$)=(6.3 mas yr⁻¹, -4.2 mas yr⁻¹), measured by astrometric observations with the Very Large Array (VLA) (Goddi et al. 2011), the derived proper motion vectors with respect to Source I point toward west and southwest directions as drawn in the black arrows in Figure 6. The magnitude of the proper motions range from 2.7 to 11.4 mas yr⁻¹ or from 5 to 23 km s⁻¹ (Table 1). Similar to the previous reports (Shimoikura et al. 2005; Hirota et al. 2011) the supermaser features are elongated along the northwest-southeast direction perpendicular to the low-velocity outflow (Genzel et al. 1981; Hirota et al. 2007; Plambeck et al. 2009; Zapata et al. 2012; Niederhofer et al. 2012; Greenhill et al. 2013; Kim et al. 2014). Observed proper motions with respect to Source I are almost perpendicular to the major axis of each feature.

The size of the maser spot at the peak channel on the maximum epoch, 2012/164, is 2.265 ± 0.014 mas \times 0.950 ± 0.006 mas (0.95 AU \times 0.40 AU) obtained from a Gaussian fitting on the self-calibrated image. The peak flux density is $(1.029 \pm 0.010) \times 10^5$ Jy, corresponding to the brightness temperature of 1.2×10^{14} K. The isotropic luminosity is estimated to be $2.4 \times 10^{-4} L_\odot$ by assuming a linewidth of 0.6 km s⁻¹.

3.4. Submillimeter observations with ALMA

To study physical and chemical properties of the supermaser, we utilize ALMA cycle 0 data to make images of submillimeter continuum emissions and molecular lines at band 7. First, we have searched for any 321.225656 GHz H₂O line signal toward the Compact Ridge where the supermaser resides for the 321.20-321.25 GHz range, as shown in Figure 8. Several spectral lines are seen, but they are identified as the HCOOCH₃ lines. If the 321 GHz H₂O line is excited by the maser action like that at 22 GHz, it should be much more compact than those of other molecular lines. With this in mind, we then investigate spectra of the H₂O lines by using the visibility data with the baseline length longer than 100 k λ , corresponding to the angular size of the emission region of $< 2''$. As a result, we can resolve out all of the lines in the Compact Ridge while a significant fraction of the 321 GHz H₂O line. In contrast, the broad 321 GHz H₂O line is clearly seen in Source I with a double peaked profile (Hirota et al. 2014a). The 321 GHz H₂O line remains in Source I even with the baselines longer than 200 k λ suggesting a compact structure (Hirota et al. 2014a). Thus, we conclude that no clear evidence of the 321 GHz H₂O maser is detected at the position of the supermaser in spite of the extraordinary strong emission of the 22 GHz H₂O maser. We note that in the observed spectral range a vibrationally excited ($\nu_2=1, 5_{2,3}-6_{1,6}$) H₂O line at 336.227931 GHz is not detected in the Compact Ridge. Non-detection of the 321 GHz and 336 GHz H₂O lines implies that the physical conditions around the Compact Ridge are certainly different from those in Source I (Hirota et al. 2014a).

We next compare the distribution of the molecular gas in the Compact Ridge which hosts the supermaser. For this purpose, we employ the HCOOCH₃ line at 321.22338 GHz

($v_t=0$, $28_{3,26}-27_{3,25}$ A), which is close to the frequency of the 321 GHz H₂O line (Figure 8), as a tracer of the dense molecular gas in the Compact Ridge (Favre et al. 2011). The 321.223 GHz HCOOCH₃ line is not blended with other HCOOCH₃ transitions unlike those at 321.229 GHz ($v_t=1$) lines, and hence, it is more suitable to analyze the velocity structure of the molecular gas. Figure 9(a) shows the moment 0 (integrated intensity) map of the 321.223 GHz HCOOCH₃ line superposed on the ALMA band 7 continuum emission. The supermaser is located at 8'' southwest of Source I and is coincident with the Compact Ridge. The position of the supermaser is close to the HCOOCH₃ peak but is rather located at the edge of the HCOOCH₃ condensation. As can be seen in the moment 1 (peak velocity) map in Figure 9 (b), the velocity of the supermaser $\sim 6.9-7.5$ km s⁻¹ is slightly blue-shifted compared with that of the HCOOCH₃ line. Furthermore, the moment 2 (velocity width) map in Figure 9 (c) implies that the linewidth of the HCOOCH₃ line tends to be broader around the supermaser. We stress that the velocity structure seems to change abruptly around the supermaser.

These apparent velocity structures are caused by two different velocity components of the molecular gas traced by the HCOOCH₃ line. In Figure 10, we can see detailed velocity structures in the Compact Ridge by the position-velocity diagram along the X and Y axes as indicated in Figure 9 (a). It is clear that there exist two different velocity components at 7.5 km s⁻¹ and 9.0 km s⁻¹. These two components were identified in the previous observations (Favre et al. 2011), but we can resolve both the velocity and spatial structures by higher spectral and spatial resolutions with ALMA. The supermaser is thought to be associated with one of them at 7.5 km s⁻¹. Interestingly, the velocity of the weak emission from the HCOOCH₃ line in Figure 10 ranges from ~ 6 to 12 km s⁻¹, although the linewidths of the HCOOCH₃ lines are only about 1 km s⁻¹ as shown in Figure 8. The velocity range of the weak HCOOCH₃ emission is significantly broader at X=0'' and Y=0'', corresponding to the position of the supermaser (see Figure 10). This is probably an evidence of a shock front at the position close to the supermaser. Indeed, possible effects of shocks in the Compact Ridge have been suggested by the enhancement of organic molecules such as HCOOH (Liu et al. 2002), HCOOCH₃ (Favre et al. 2011), and CH₃OCH₃ (Brouillet et al. 2013).

Figure 11 shows a close-up view of distributions of the ALMA band 7 continuum emission superposed on the integrated intensity map of the 321.223 GHz HCOOCH₃ line (Figure 9(a)). Positions of the 22 GHz H₂O masers (Gaume et al. 1998) including that of the supermaser are also indicated. We detect the compact continuum emission both at ALMA bands 6 and 7 (Hirota et al. 2014b). The accurate position of the supermaser is significantly shifted from the continuum peak by 0.3'' southeast. We also indicate positions of other possible counterparts observed previously. Their relationship will be discussed in the next section.

4. Discussion

In this paper, we report results of continued monitoring observations of the supermaser with VERA for more than 5 years. We also acquire follow-up observational data with ALMA of submillimeter continuum emissions and H₂O lines at 321 GHz to reveal characteristics of the supermaser and their environments. In this section, we will address following issues related to the supermaser: What is the powering source of the supermaser and what makes the 6.9 and 7.5 km s⁻¹ features in the Compact Ridge only such a special burst event? Why there is no bursting H₂O maser feature at 321 GHz despite the extraordinary high flux density in the 22 GHz H₂O maser? How the drastic burst of the H₂O maser can be explained? Is there a periodicity of the burst event?

4.1. Possible powering source of the supermaser

According to the absolute position of the supermaser derived from our VERA observations, we propose that the supermaser would be excited in the shocked molecular gas interacting between the low-velocity outflow driven by Source I and ambient dense gas in the Compact Ridge (Genzel et al. 1981; Hirota et al. 2011). Proper motions and elongations of the supermaser features (Figure 6) and the broader HCOOCH₃ line at the position of the supermaser (Figure 10) support this scenario. It has also been suggested by the fact that the H₂O maser tends to be distributed in the interface of the shocked molecular gas in the Compact Ridge traced by HCOOH (Liu et al. 2002) and HCOOCH₃ (Favre et al. 2011) lines. Furthermore, Favre et al. (2011) point out a possible relation between the Compact Ridge and an explosive outflow traced by the CO lines (Beuther & Nissen 2008; Zapata et al. 2009). Indeed, the supermaser is found to be located at the edge of the low-velocity bipolar molecular outflow traced by the thermal SiO lines (Plambeck et al. 2009; Zapata et al. 2012; Niederhofer et al. 2012) as well as the explosive outflow (Beuther & Nissen 2008; Zapata et al. 2009). The latter one is thought to be the result of a recent close encounter of Source I and BN object (Bally et al. 2011; Goddi et al. 2011), although a relationship between these two outflows is still unclear.

Note that an infrared source IRc 5 is located at 1'' southeast of the supermaser. The position of IRc 5 corresponds to a nearby 3 mm continuum peak, C29 (Friedel & Weaver 2011), and an HCOOCH₃ peak, MF14 (Favre et al. 2011) and hence, it is more closely related to these sources. Since IRc 5 is thought to be a shocked molecular gas heated externally (Okumura et al. 2011), it would not be directly related to the excitation of the supermaser. Alternatively, both of them are thought to be heated by the common outflow.

As discussed previously (Hirota et al. 2011), however, it has been still unknown why only the 6.9 km s⁻¹ and 7.5 km s⁻¹ features show such an extraordinary burst phenomenon. One of the possible explanations is a special physical or geometrical condition of the maser excitation in this region. An anomalous amplification of the H₂O maser burst might need a long path length. Such a condition could be achieved only in the systemic velocity component.

Because it can supply plenty of ambient molecular gas within a narrow velocity range, maser emission would be efficiently amplified only close to the systemic velocity (Hirota et al. 2011). Millimeter and submillimeter continuum emissions are detected by Tang et al. (2010), SMM1 in Zapata et al. (2011) and Cb1 in Favre et al. (2011) with spatial resolution of $\sim 0.8\text{--}3''$. The mass of the submillimeter core in the Compact Ridge is estimated to be $4M_{\odot}$ (Tang et al. 2010), and hence, they could provide the dense gas required to form new stars. A similar conclusion is obtained from the ALMA Science Verification continuum data that have been analyzed by Brouillet et al. (2014).

To account for a necessary condition for the supermaser, it is also suggested that the maser burst could occur as a result of an interaction with outflows and a pre-existing YSO in the Compact Ridge (Garay et al. 1989). As discussed in detail by Favre et al. (2011), there are possible candidate sources physically associated with the supermaser; a radio continuum source labeled R detected with VLA (Felli et al. 1993), 3 mm continuum emission sources detected with the Combined Array for Research in Millimeter-wave Astronomy (CARMA) (Friedel & Weaver 2011), molecular peaks traced by HCOOCH_3 lines with the IRAM Plateau de Bure interferometer (PdBI) (Favre et al. 2011), and optical source Parenago 1822, which is also identified from millimeter, near infrared, optical and X-ray (see SIMBAD), in the Compact Ridge (Figure 11).

Eisner et al. (2008) detect a compact 1.3 mm continuum source named HC 438 in the Compact Ridge with a flux density of 67.8 ± 14.2 mJy by using CARMA. We also detect a compact continuum source at ALMA band 7 (see contours in the middle of Figure 11) which is also detected at Band 6 (Hirota et al. 2014b). These observations achieve much higher spatial resolution of $\sim 0.5''$ than those reported above (Tang et al. 2010; Zapata et al. 2011; Favre et al. 2011). The flux density at ALMA bands 6 and 7 are 57 ± 5 mJy and 129 ± 14 mJy, respectively (Hirota et al. 2014b). The ALMA band 6 result is consistent with that of the CARMA 230 GHz observation (Eisner et al. 2008). The supermaser is located within the submillimeter core detected by ALMA but is shifted by $0.3''$ from the peak position. Taking into account positional uncertainties, they are identical to HC 438 (Eisner et al. 2008), the 3 mm continuum source C32 (Friedel & Weaver 2011) and HCOOCH_3 peak MF1 (Favre et al. 2011). The circumstellar mass of HC 438 is derived to be $0.085 M_{\odot}$ with the assumed dust temperature of 20 K (Eisner et al. 2008). If we assume a higher temperature of 100 K derived from the HCOOCH_3 data (Favre et al. 2011), the smaller mass of $0.01M_{\odot}$ is obtained. These mass estimates would be a lower limit of the dust continuum source possibly associated with the supermaser because most of the flux is filtered out by ALMA and CARMA with extended configurations.

We speculate that an embedded YSO associated with jet/outflow/disk (Matveenko et al. 1988; Matveyenko et al. 2004; Shimoikura et al. 2005; Eisner et al. 2008) would play an important role to realize special conditions required for the supermaser. We notice that the

H₂O maser features near the supermaser detected with VLA (Gaume et al. 1998) are distributed around the submillimeter continuum peak as seen in Figure 11. It may imply an expanding shell ejected by an embedded YSO, which are sometimes seen in massive YSOs (Torrelles et al. 2003). As discussed in section 3.1, we tried to search for other maser features in Orion KL region previously detected with VLA (Gaume et al. 1998). We made channel maps of the H₂O maser features with VERA within an 1'' \times 1'' field of view around the supermaser in the Compact Ridge. However, we found no maser emission because of the limited dynamic range seriously affected by the extremely strong supermaser. Further observations of continuum emission and H₂O masers with higher dynamic range will unveil the exact location of the embedded YSO in the Compact Ridge.

4.2. Implication for the pumping mechanism

It is proposed that the pumping mechanism of the H₂O maser is dominated by collisional excitation (Elitzur et al. 1989; Neufeld & Melnick 1990; Neufeld & Melnick 1991). The burst of the H₂O maser in Orion KL is proposed as the result of collisional pumping in the magnetohydrodynamic shock wave caused by the outflow (Garay et al. 1989). On the other hand, alternative mechanisms are also considered to account for the extraordinary H₂O maser burst, such as overlapping of two maser gas clumps (Deguchi & Watson 1989; Shimoikura et al. 2005) and accidental beaming of radiation toward the Earth rather than a change in excitation (Genzel et al. 1981). To constrain the physical properties of the supermaser, we have carried out observations of the submillimeter H₂O lines which could be masing (Neufeld & Melnick 1990; Neufeld & Melnick 1991) by using ALMA. Among a number of H₂O lines, we employ the 10_{2,9}-9_{3,6} transition at 321 GHz which is proposed to be a good indicator of some key parameters including temperature, density, and H₂O abundance in the masing gas clump (Neufeld & Melnick 1990).

However, there is no significant emission of the 321 GHz H₂O line at the position around the supermaser. The upper limit of the flux density of the 321 GHz H₂O line is ~ 0.1 Jy. If we assume physical properties of the masing gas are common for both the 22 GHz and 321 GHz lines, then a photon luminosity ratio, $L_p(22 \text{ GHz})/L_p(321 \text{ GHz})$, is identical to the observed flux density ratio, $F(22 \text{ GHz})/F(321 \text{ GHz})$. Then, an upper limit of $L_p(22 \text{ GHz})/L_p(321 \text{ GHz}) > 10^6$ is obtained from the flux density of the 22 GHz maser of $> 10^5$ Jy. When the beaming angle of the 22 GHz maser is also the same as that of 321 GHz, an emissivity ratio $R \equiv Q(22 \text{ GHz})/Q(321 \text{ GHz})$ (Neufeld & Melnick 1990) is also equal to the photon luminosity ratio and flux density ratio, $R > 10^6$.

As demonstrated in the model calculations (Neufeld & Melnick 1990), the lower limit of $R > 10^6$ can be achieved when the temperature is ~ 200 -400 K or the parameter $\log \xi$ is ~ 0.4 -1.8 depending on the temperature within the calculated range below 2000 K (see their Figure 3). The parameter ξ is defined as $\xi \equiv x_{-4}(\text{H}_2\text{O}) n_9^2 / (dv_z/dz)_{-8}$, in which $x_{-4}(\text{H}_2\text{O})$,

n_9 , and $(dv_z/dz)_{-8}$ are a fractional abundance of H₂O relative to hydrogen nuclei in units of 10⁻⁴, a number density of hydrogen nuclei in units of 10⁹ cm⁻³, and a velocity gradient in units of 10⁻⁸ cm s⁻¹ cm⁻¹ (Neufeld & Melnick 1990). We note that the model employed here is calculated under the assumption of a saturated maser (Neufeld & Melnick 1990) and hence, the estimated parameters may be different from an unsaturated case as adopted for the supermaser. Furthermore, the model calculation only considers collisional pumping of H₂O molecules ignoring infrared pumping. In addition, the collision rates used in these works are now superseded by newer calculations (Daniel & Cernicharo 2013). Despite these uncertainties, we use the model of Neufeld & Melnick (1990) to roughly interpret the supermaser burst at 22 GHz and the non-detection of the 321 GHz line. As a result, we find the supermaser burst at 22 GHz and the non-detection at 321 GHz could still be explained by the theoretical model (Neufeld & Melnick 1990) without extraordinary physical conditions. Thus, under the condition of the unsaturated 22 GHz H₂O maser, the lower temperature and larger value of ξ would also be expected according to a qualitative consideration.

To explain the non-detection of the 321 GHz maser line (high value of $R \sim \infty$), either high H₂O abundance, high H₂ density, small velocity gradient, or low temperature of 200-400 K would be required. The H₂O abundance in the Compact Ridge is estimated from the Herschel data to be 2.6×10^{-6} with the source size of 6'' (Neill et al. 2013). If a local abundance enhancement occurs around the supermaser, the higher H₂O abundance up to 6.5×10^{-4} as observed in the Hot Core region (Neill et al. 2013) may be possible. The average H₂ number density of the dust continuum source in the Compact Ridge is estimated to be $(0.5-5) \times 10^9$ cm⁻³ assuming a diameter (FWHM) of 0.43'' or 90 AU (Hirota et al. 2014b) and a total mass of 0.01-0.1 M_\odot (Eisner et al. 2008; Hirota et al. 2014b). If we assume a velocity width of 0.6 km s⁻¹ and a path length of 1 AU as obtained from a Gaussian fitting for a bursting maser spot, the velocity gradient $(dv_z/dz)_{-8}$ is calculated to be 0.4. Although the above results contain large uncertainties by a factor of 10 or more, these parameters seem reasonable to explain estimated range of $\log \xi$ of 0.4-1.8 unless the H₂O abundance is the lowest estimate of $x_{-4}(\text{H}_2\text{O})=0.026$ (Neill et al. 2013).

It is also conceivable that the supermaser is the result of strong beaming effects (Genzel et al. 1981). If only the 22 GHz maser emission has a smaller beaming angle compared with that of the 321 GHz line, the emissivity ratio R is proportional to the flux density ratio, $F(22 \text{ GHz})/F(321 \text{ GHz})$, and the ratio of beaming angles, $\Omega(22 \text{ GHz})/\Omega(321 \text{ GHz})$, which reduces the upper limit of R estimated from the observed flux density ratio. The smaller beaming angle of the 22 GHz maser line than that of 321 GHz by a factor of ~ 100 would enable a large $\Omega(22 \text{ GHz})/\Omega(321 \text{ GHz})$ value of ~ 10000 . This may result in the lower R value by a factor of 10000 which can be achieved under wider range of physical conditions as seen in Figure 3 of Neufeld & Melnick (1990).

In spite of the presence or absence of a beaming effect, the condition for the H₂O maser

burst only at the 22 GHz transition, $R > 10^6$, does not require extreme physical properties but rather those typical in hot molecular cores (Neill et al. 2013). We suggest that the symmetric time variation in the flux density (Figure 3) could be explained by a change in the beaming angle of the maser rather than changes in the physical properties such as H₂O abundance, H₂ density, and/or temperature. On the other hand, a change in a velocity gradient caused by a length of the maser cloud and/or velocity structure might happen such as those in the overlapping maser model (Deguchi & Watson 1989; Shimoikura et al. 2005). Nevertheless, it is still uncertain how such an accidental overlapping and/or a beaming effect could occur in two spatially distinct clouds for several times during our monitoring period of ~ 5 years.

4.3. Periodicity and lifetime of the H₂O maser burst

Comparing the basic properties such as the peak LSR velocity, the spatial structure of each feature, and the location coincident with the Compact Ridge, all of the burst events in 1979-1985, 1998-1999, and 2011-2012 could have a common origin. It is also suggested that the H₂O maser burst may have periodicity of 13 years (Tolmachev 2011). However, the current burst shows less activities in terms of the maximum flux density. Furthermore, no such burst event is reported in 1973 (Baudry et al. 1974), in which the burst event is expected if 13 year-periodicity is valid (i.e. 1972-1973, 1979-1985, 1998-1999, and 2011-2012). In 1973 July, the observed flux density of the H₂O maser at 7.4 km s⁻¹ was only about 100 Jy and was weaker than the 11.0 km s⁻¹ component (Baudry et al. 1974). This component was probably identical to the second brightest component in the current burst phase (Figure 1). The position of the 7.4 km s⁻¹ component was measured to be R.A.=05h35m14.22s and decl.=-05°22'37".0 (J2000) and was consistent with that of the current bursting feature located in the Compact Ridge. In 1975-1976, the H₂O maser feature at 7.6 km s⁻¹ was detected at the position of R.A.=05h35m14.07s and decl.=-05°22'38".0 (J2000). The position of this feature was again in good agreement with that of the current H₂O maser burst, whereas it was rather weak (much less than 1000 Jy) compared with another strong feature at 10.8 km s⁻¹.

Although the H₂O maser feature at ~ 7.5 km s⁻¹ could be excited by a common origin in the Compact Ridge, it is not very likely that the maser burst occurs regularly at a period of 13 years. More archive data of past observations will be helpful to investigate a long-term variability of the H₂O maser activities since early 1970s. The flux increase started in 2013 is now on-going and hence, further monitoring will also provide some hints to understand a possible relation with previous bursts. Along with the 22 GHz H₂O maser lines, it could be useful to continue monitoring observations of the 321 GHz H₂O lines in Orion KL with ALMA in order to see whether the Compact Ridge and Source I, which is a powering source of the outflow interacting with the Compact Ridge, behave in the same way.

Figures 1-3 imply that the current burst in 2011 and 2012 sometimes shows variations in the flux density and velocity structure with the timescales of 2-7 months. It is comparable to

those of typical H₂O masers in Orion KL (Hirota et al. 2007). Although the spectral component of the supermaser seems to survive for more than 5-10 years (Genzel et al. 1981; Garay et al. 1989), a spatial structure of each bursting feature is found to be changing within a timescale of a few months to <2 years at the longest lifetime (Table 1). Thus, it is unlikely that the bulk of the bursting maser gas is identical for longer than ~ 2 years.

5. Summary

We have carried out astrometric monitoring observations of the bursting 22 GHz H₂O maser feature, called supermaser, in Orion KL using VERA since 2011 March. Combined with spectral line data obtained as a fringe-finder, we reveal a time variation of the supermaser for more than 5 years. In addition, we utilize ALMA cycle 0 data at band 7 (320-330 GHz) for both spectral lines and continuum emissions to investigate physical and chemical properties of the supermaser. The main findings are summarized as follows:

1. Within the monitoring period in 2011 and 2012, we detect three active phases with rising and falling timescales ranging from 2 to 7 months. We also find a smaller burst in 2009 with a slightly longer rising and falling timescales of ~ 10 months. The flux variations of the supermaser seem to be symmetric in time for all of the active phases.
2. The maximum phase of the current burst is observed on 2012/154 with the total flux density of 135000 Jy, which is one order of magnitude lower than those in previous bursts. Although the burst events may occur with a possible periodicity of 13 years, (i.e. 1979-1985, 1998-1999, and 2011-2012), a lower flux density by a factor of 10 in the current burst, as well as no significant burst event in 1973 (Baudry et al. 1974) would make the claimed periodicity of 13 years still unconvincing.
3. The outburst of the maser emission can be seen in two velocity components at ~ 6.9 km s⁻¹ and ~ 7.5 km s⁻¹ as reported in Garay et al. (1989) and Hirota et al. (2011). The 6.9 km s⁻¹ feature is alive only in 2011 with the lifetime of ~ 8 months. Note that we detect two spatially distinct features at 6.9 km s⁻¹ and 7.5 km s⁻¹, and hence, these two velocity components are unlikely due to the hyperfine structure of the H₂O molecule.
4. The flux density and linewidth show an anti-correlation as expected for an unsaturated maser emission (Goldreich & Kwan 1974), in which the logarithm of the flux density of the maser line, $\log F$, is proportional to the inverse square of the linewidth, Δv^{-2} . However, we cannot rule out a possibility of a saturated maser case because such a line narrowing is also predicted to occur even for a saturated maser if a stimulated emission rate is not large compared with that of the cross-relaxation (Goldreich & Kwan 1974).
5. As reported in previous papers (Shimoikura et al. 2005; Hirota et al. 2011) the bursting maser features are elongated along the northwest-southeast direction perpendicular to the low-velocity outflow driven by Source I. Absolute proper motions of the bursting maser features are measured based on a longer monitoring period than that in the previous paper

(Hirota et al. 2011). Their proper motions with respect to a powering source of the low-velocity outflow, Source I, are almost perpendicular to the elongation of the maser features, suggesting that they are related to the low-velocity outflow.

6. The size of the maser spot at the peak channel on the maximum epoch, 2012/164, is $2.265 \text{ mas} \times 0.950 \text{ mas}$, and the total flux density is $1.029 \times 10^5 \text{ Jy}$. These values correspond to the brightness temperature and the isotropic luminosity of $1.2 \times 10^{14} \text{ K}$ and $2.4 \times 10^{-4} L_{\odot}$, respectively.
7. The supermaser is located at the Compact Ridge region in Orion KL. Continuum peaks detected by ALMA bands 6 and 7 are located $0.3''$ northwest of the supermaser. As suggested by Favre et al. (2011), there are a radio continuum source labeled R (Felli et al. 1993), 3 mm continuum source C32 (Friedel & Weaver 2011), HCOOCH₃ core MF1 (Favre et al. 2011), and optical source Parenago 1822, which are probably identical or closely related to the compact continuum sources detected by ALMA and the supermaser.
8. The position of the supermaser is coincident with the dense gas traced by the HCOOCH₃ line. The velocity of the supermaser agrees well with one of the two velocity components of the HCOOCH₃ line detected by ALMA and PdBI (Favre et al. 2011). A slightly broader velocity range of the weak HCOOCH₃ emission would imply a shock front at the position of the supermaser.
9. The 321 GHz H₂O line is not detected around the 22 GHz supermaser features, although the strong maser emission is found to be associated with Source I (Hirota et al. 2014a). Given the high emissivity ratio, the maser burst at 22 GHz could occur under conditions of the temperature of $<200\text{-}400 \text{ K}$ and/or the parameter $\log \xi \sim 0.4 - 1.8$, suggesting a high abundance of H₂O, a high number density of H₂, and/or a small velocity gradient. Meanwhile, these physical properties are not extraordinary values but are very similar to typical hot molecular cloud cores. Thus, the supermaser burst at 22 GHz with non-detection of the 321 GHz maser emission could be explained by the theoretical model qualitatively (Neufeld & Melnick 1990). Further detailed calculations would be required to interpret the observed flux ratios of the masers (Daniel & Cernicharo 2013).
10. Alternatively, the supermaser may be caused by an accidental beaming only for the 22 GHz H₂O maser (Genzel et al. 1981). The symmetric time variation in the flux density is consistent with a result of the beaming rather than changes in physical properties of the masing gas. However, it still remains a matter of debate how accidental overlapping and/or beaming occur repetitively for more than ~ 30 years since the discovery of the supermaser.

We are grateful to Alain Baudry for useful comments, which is essential to improve our scientific discussion. We thank the staff of the VERA stations and ALMA observatory to support our project. This paper makes use of the following ALMA data: ADS/JAO.ALMA#2011.0.00199.S. ALMA is a partnership of ESO (representing its member

states), NSF (USA) and NINS (Japan), together with NRC (Canada) and NSC and ASIAA (Taiwan), in cooperation with the Republic of Chile. The Joint ALMA Observatory is operated by ESO, AUI/NRAO and NAOJ. This research has made use of the SIMBAD database, operated at CDS, Strasbourg, France. T.H. is supported by the MEXT/JSPS KAKENHI Grant Numbers 21224002, 24684011, and 25108005, and the ALMA Japan Research Grant of NAOJ Chile Observatory, NAOJ-ALMA-0006. M.H. is supported by the MEXT/JSPS KAKENHI Grant Numbers 24540242 and 25120007.

References

- Allen, D. A. & Burton, M. G. 1993, *Nature*, 363, 54
- Bally, J. 2008, in *Handbook of Star Forming Regions*, Vol. 1, ed. B. Reipurth (ASP Monograph Publications, Vol. 4; San Francisco, CA: ASP), 459
- Bally, J., Cunningham, N. J., Moeckel, N., Burton, M. G., Smith, N., Frank, A., & Nordlund, A. 2011, *ApJ*, 727, 113
- Baudry, A., Forster, J. R., & Welch, W. J. 1974, *A&A*, 36, 217
- Beuther, H., & Nissen, H. D. 2008, *ApJL*, 679, L121
- Brouillet, N., Despois, D., Baudry, A., et al. 2013, *A&A*, 550, 46
- Brouillet, N. et al. 2014, in preparation
- Chen, P., Pearson, J. C., Pickett, H. M., Matsuura, S., & Blake, G. A. 2000, *ApJS*, 128, 371
- Churchwell, E., Felli, M., Wood, D. O. S., & Massi, M. 1987, *ApJ*, 321, 516
- Daniel, F. & Cernicharo, J. 2013, *A&A*, 553, A70
- Deguchi, S. & Watson, W. D. 1989, *ApJL*, 340, L17
- Eisner, J. A., Plambeck, R. L., Carpenter, J. M., Corder, S. A., Qi, C., & Wilner, D. 2008, *ApJ*, 683, 304
- Elitzur, M., Hollenbach, D. J., McKee, C. F. 1989, *ApJ*, 346, 983
- Favre, C., Despois, D., Brouillet, N., Baudry, A., Combes, F., Guélin, M., Wootten, A., & Wlodarczak, G. 2011, *A&A*, 532, A32
- Felli, M., Churchwell, E., Wilson, T. L., Taylor, G. B. 1993, *A&AS*, 98, 137
- Forster, J. R., Welch, W. J., Wright, M. C. H., & Baudry, A., 1978, *ApJ*, 221, 137
- Friedel, D. N. & Widicus Weaver, S. L. 2011, *ApJ*, 742, 64
- Garay, G., Moran, J. M., & Haschick, A. D. 1989, 338, 244
- Gaume, R. A., Wilson, T. L., Vrba, F. J., Johnston, K. J., Schmid-Burgk, J. 1998, *ApJ*, 493, 940
- Genzel, R., Reid, M. J., Moran, J. M., & Downes, D. 1981, *ApJ*, 244, 884
- Genzel, R., & Stutzki, J. 1989, *ARAA*, 27, 41
- Goddi, C., Humphreys, E. M. L., Greenhill, L. J., Chandler, C. J., & Matthews, L. D. 2011, *ApJ*, 728, 15
- Goldreich, P. & Kwan, J. 1974, *ApJ*, 190, 27
- Greenhill, L. J., Goddi, C., Chandler, C. J., Matthews, L. D., Humphreys, E. M. L. 2013, *ApJ*, 770, 32
- Hirota, T., Tsuboi, M., Fujisawa, K. et al. 2011, *ApJ*, 739, L59

Hirota, T., Bushimata, T., Choi, Y. K. et al. 2007, PAJS, 59, 897

Hirota, T., Kim, M. K., Kurono, Y., & Honma, M. 2014a, ApJL, 782, L28

Hirota, T., Kim, M. K., Kurono, Y., & Honma, M. 2014b, in preparation

Kaifu, N., Usuda, T., Hayashi, S. et al. 2000, PASJ, 52, 1

Kim, M. K., Hirota, T., Honma, M., et al. 2008, PASJ, 60, 991

Kim, M. K., Hirota, T., Honma, M., & Kobayashi, H. 2014, in preparation

Kukolich, S.G. 1969, J. Chem. Phys., 50, 3751

Liu, S. -Y., Girart, J. M., Remijan, A., & Snyder, L. E. 2002, ApJ, 576, 255

Ma, C., Arias, E. F., Eubanks, T. M., et al. 1998, AJ, 116, 516

Matthews, L. D., Greenhill, L. J., Goddi, C., Chandler, C. J., Humphreys, E. M. L., & Kunz, M. W. 2010, ApJ, 708, 80

Matveenko, L. I., Graham, D. A., & Diamond, P. J. 1988, Sov. Astron. Lett., 14, 468

Matveyenko, L. I., Zhakharin, K. M., Diamond, P. J., & Graham, D. A. 2004, Astron. Lett., 30, 100

Matveyenko, L. I., Demichev, V. A., Ipatov, A. V., Melnikov, A. E., & Surkis, I. F. 2012a, AstL, 38, 575

Matveyenko, L. I., Demichev, V. A., Ipatov, A. V., Melnikov, A. E., & Surkis, I. F. 2012b, AstL, 38, 764

Menten, K. M., & Reid, M. J. 1995, ApJ, 445, L157

Menten, K.M., Reid, M. J., Forbrich, J., & Brunthaler, A. 2007, A&A, 474, 515

Neill, J., L., Wang, S., Bergin, E. A., Crockett, N. R., Favre, C., Plume, R., Melnick, G. J. 2013, ApJ, 770, 142

Neufeld, D. A. & Melnick, G. J. 1990, ApJL, 352, L9

Neufeld, D. A. & Melnick, G. J. 1991, ApJ, 368, 215

Niederhofer, F., Humphreys, E. M. L., & Goddi, C. 2012, A&A, 548, A69

Okumura, S., Yamashita, T., Sako, S., Miyata, T., Honda, M., Kataza, H., Okamoto, Y. K. 2011, PASJ, 63, 823

Omodaka, T., Maeda, T., Miyoshi, M., et al. 1999, PASJ, 51, 333

Otto, S. & Gaylard, M. J. 2012, in IAU Symp., 287, Cosmic Masers — from OH to H₀, ed. R. S. Booth, E. M. L. Humphreys, & W. H. T. Vlemmings (Cambridge: Cambridge Univ. Press), 110

Plambeck, R. L., Wright, M. C. H., Friedel, D. N., et al. 2009, ApJ, 704, L25

Shimoikura, T., Kobayashi, H., Omodaka, T., Diamond, P. J., Matveyenko, L. I., & Fujisawa, K. 2005, ApJ, 634, 459

Tang, Y. W., Ho, P. T. P., Koch, P. M., & Rao, R. 2010, ApJ, 717, 1262

Torrelles, J. M. et al. 2003, ApJL, 598, L115

Tolmachev, A. 2011, ATel, 3177

Zapata, L. A., Rodríguez, L. F., Schmid-Burgk, J., Loinard, L., Menten, K. M., & Curiel, S. 2012, ApJ, 754, L17

Zapata, L. A., Schmid-Burgk, J., Ho, P. T. P., Rodríguez, L. F., Menten, K. M. 2009, ApJ, 704, L45

Zapata, L. A., Schmid-Burgk, J., & Menten, K. M. 2011, A&A, 529, A24

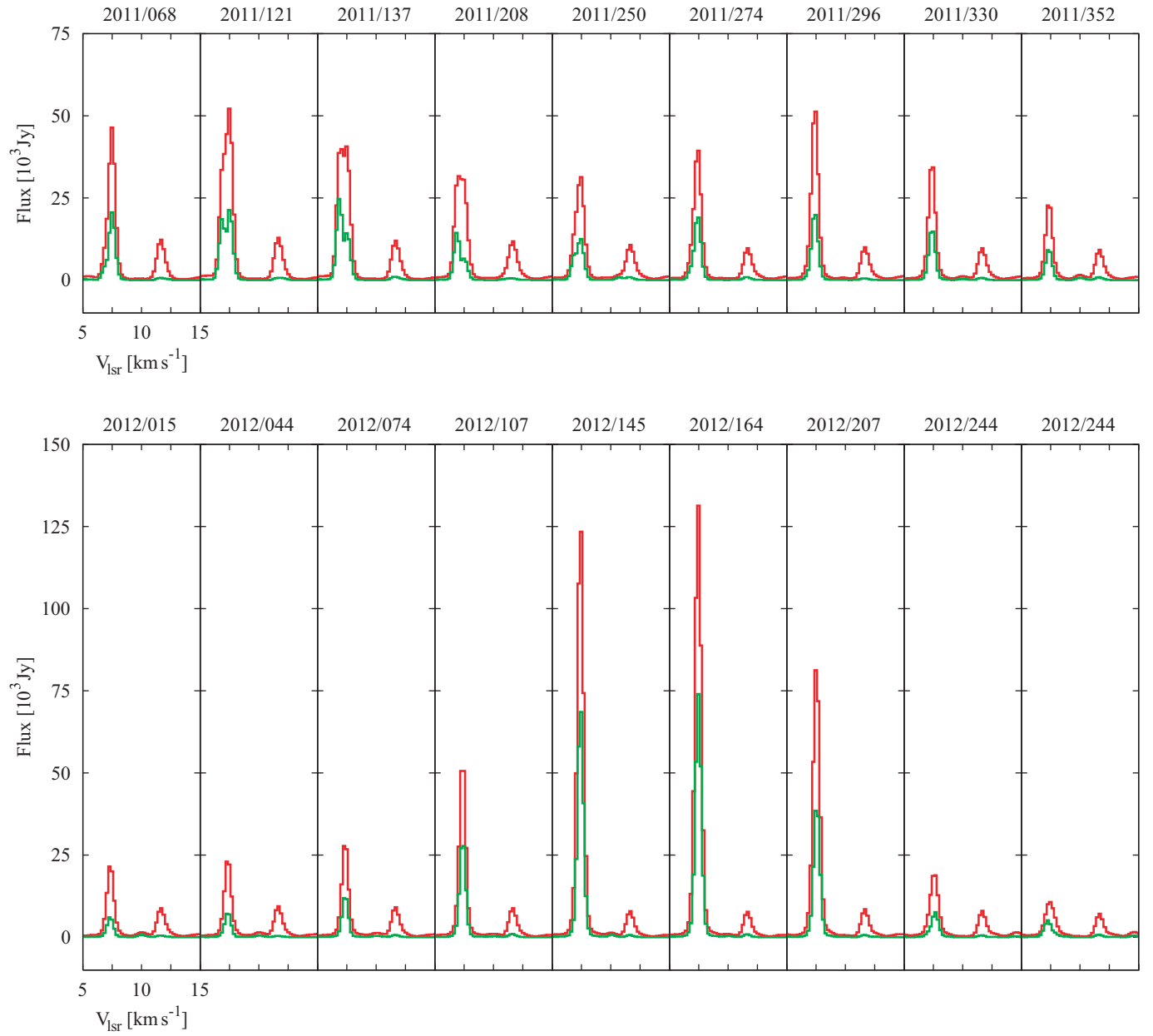


Fig. 1. Spectra of the supermaser in Orion KL observed in regular astrometry observations in 2011 and 2012. Red and green lines represent the total-power and cross-power spectra, respectively, integrated over all baselines/antennas and all scans. The observed epoch is indicated at the top of each panel.

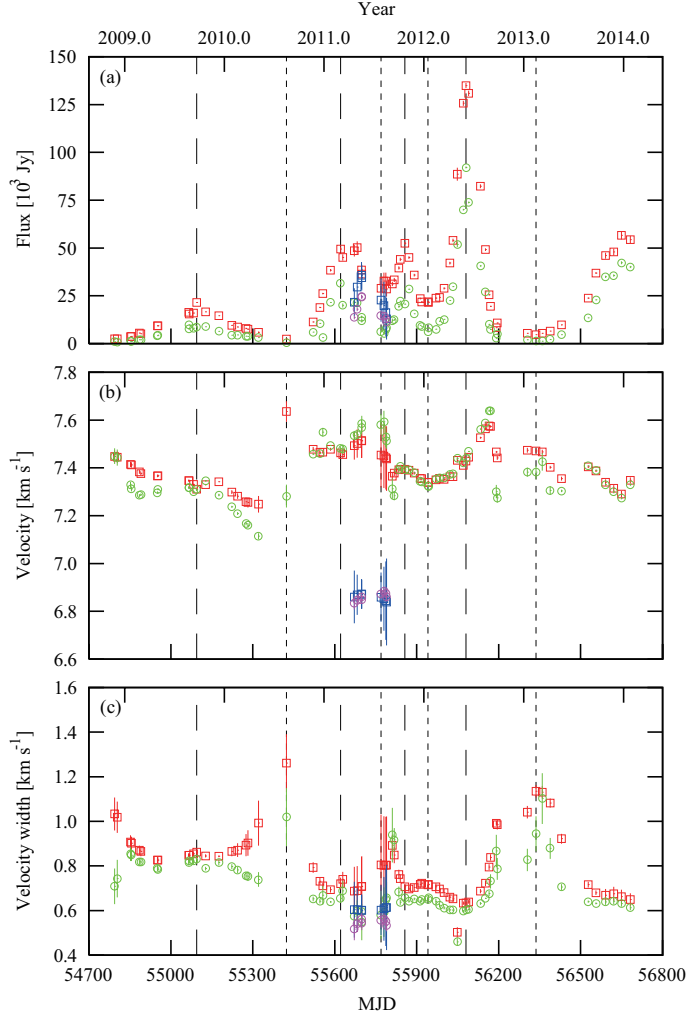


Fig. 2. Time variations of (a) total and correlated flux densities, (b) peak velocity, and (c) velocity width of the supermaser. Results of both 18 epochs of regular astrometry and 53 epochs of spectral line monitoring observations are plotted. In each panel, results of the Gaussian fitting of the total-power and cross-power spectra are indicated with the 3σ errors, although the error bars are hardly seen due to high signal-to-noise ratios. Squares and circles represent the best-fit parameters for total-power spectra and cross-power spectra, respectively. In the middle of 2011, spectra clearly show double-peaked profiles, and hence, two different Gaussian components are fitted to the observed spectra, as shown in red/green and blue/magenta for the ~ 6.9 km s $^{-1}$ and 7.5 km s $^{-1}$ components, respectively. Dashed and dotted lines represent epochs with the maximum and minimum flux densities, respectively.

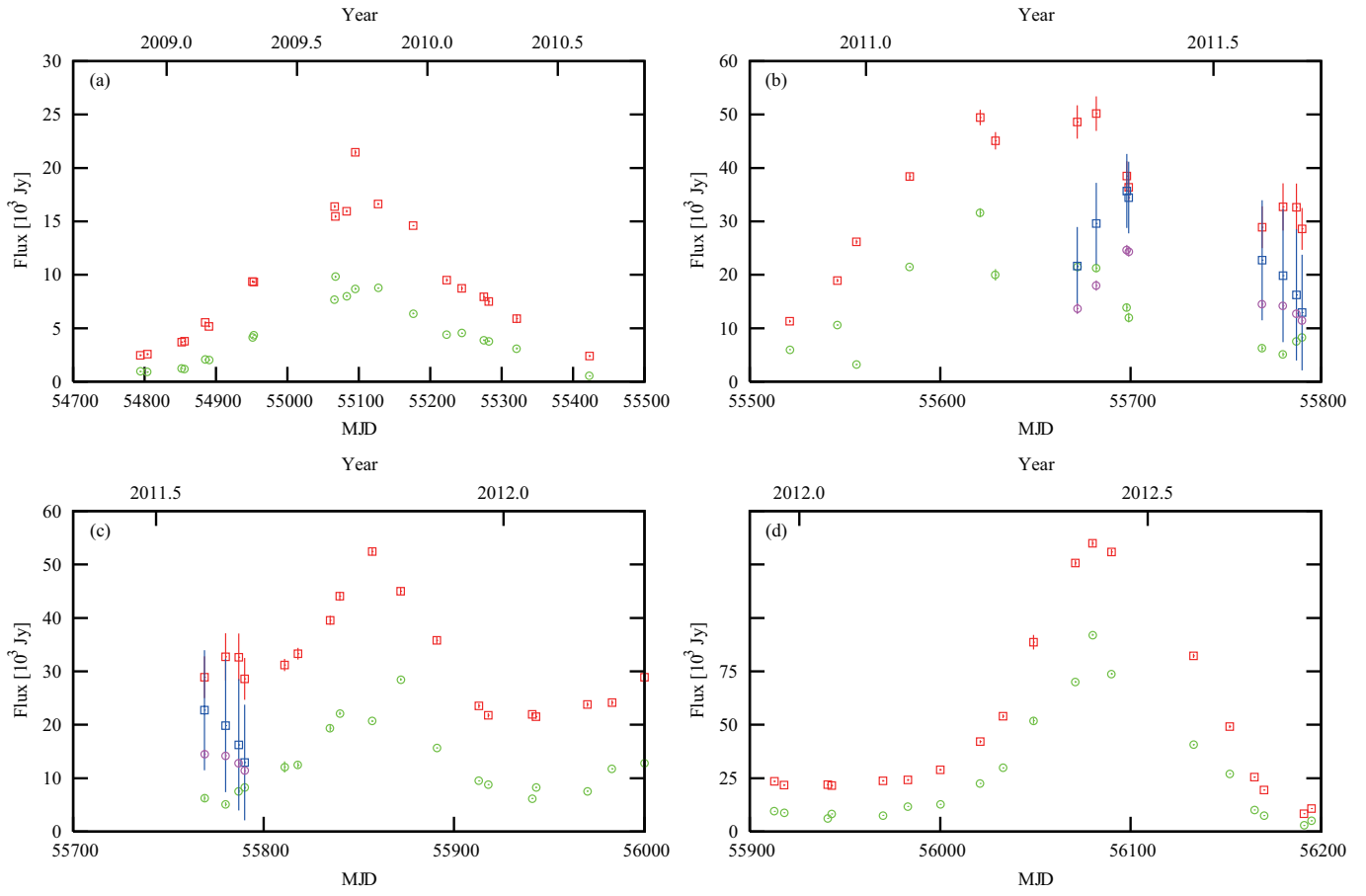


Fig. 3. Enlarged views of the flux variations for each burst as shown in Figure 2. (a) 2009-2010, (b) first burst in 2011, (c) second burst in 2011, and (d) 2012. Symbols are the same as Figure 2.

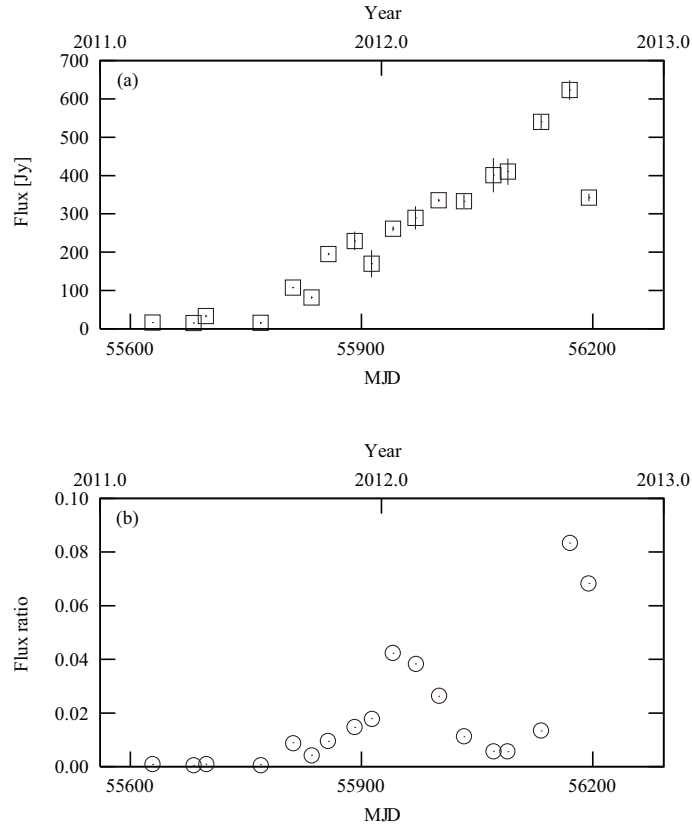


Fig. 4. Time variation of (a) the flux density of SE feature and (b) the flux density ratio relative to the supermaser feature observed in 2011 and 2012. Correlated flux density in Figure 2(a) is employed to calculate the flux density ratio. When there are two velocity components in the supermaser, sum of these flux densities is plotted.

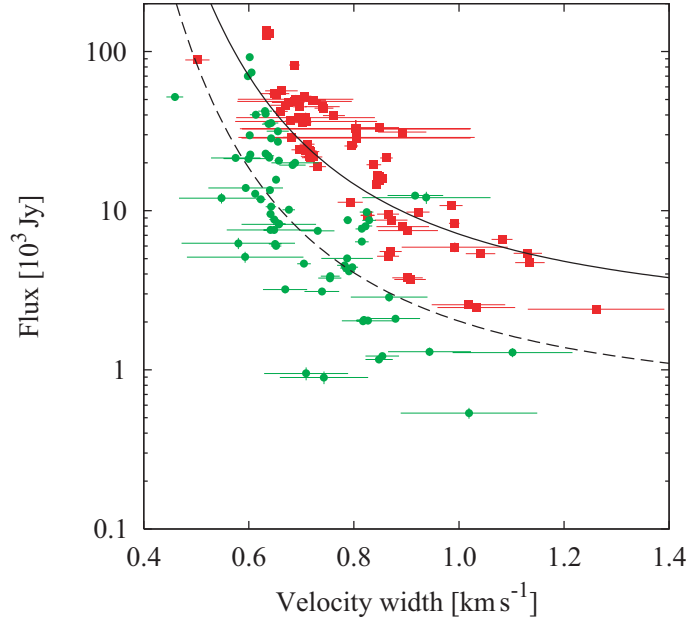


Fig. 5. Relationship between the flux density and linewidth of observed spectra of the supermaser. Red squares and green circles represent the observed values for total-power and cross-power spectra, respectively. Solid and dashed lines show best-fit results of the fitting; $\log F = A + B\Delta v^{-2}$, where parameters (A, B) are $(2.0 \pm 0.3, 1.29 \pm 0.09)$ and $(0.58 \pm 0.16, 1.25 \pm 0.12)$ for the results of total- and cross-power spectra, respectively.

Table 1. Proper motions of the detected spots.

Feature	Spot	V_{LSR}	$\mu_{\alpha} \cos \delta$	μ_{δ}	Epoch
ID ^a	ID ^b	[km s ⁻¹]	[mas yr ⁻¹]	[mas yr ⁻¹]	
1	1	6.74	-2.0(0.4)	-1.8(0.4)	2011/068-2011/296
1	3	6.95	-2.2(0.5)	-1.7(0.6)	2011/068-2011/296
1	5	7.16	-2.7(1.2)	-1.0(1.4)	2011/068-2011/250
2	2	6.74	5.2(0.9)	-10.2(0.8)	2011/296-2012/164
2	4	6.95	4.8(0.6)	-9.7(0.5)	2011/250-2012/207
2	6	7.16	4.0(0.3)	-9.0(0.2)	2011/068-2012/207
2	7	7.37	4.0(0.2)	-9.1(0.2)	2011/068-2012/207
2	8	7.58	4.0(0.2)	-9.1(0.2)	2011/068-2012/269
2	10	7.79	4.0(0.2)	-9.0(0.2)	2011/068-2012/269
3	9	7.58	-2.6(9.2)	-4.1(8.3)	2011/121-2011/208
3	11	7.79	0.6(3.7)	-5.5(3.7)	2011/121-2011/208

a: Feature IDs are defined in the previous paper (Hirota et al. 2011).

b: Spot IDs are indicated in Figure 6.

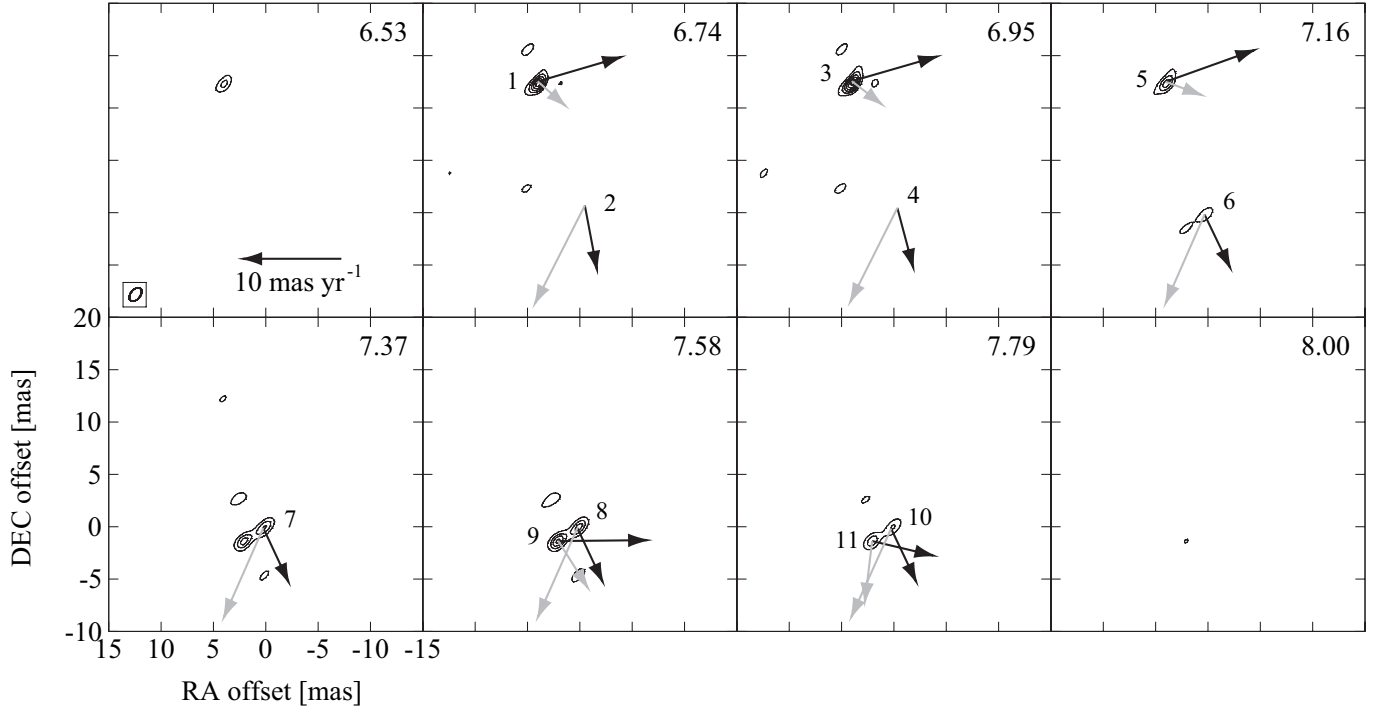


Fig. 6. Phase-referenced images of the bursting maser features at the epoch 2011/137. Absolute proper motions and proper motions with respect to Source I are indicated by gray and black arrows, respectively. Contour levels are 1, 2, 3, 4, 5, and $6 \times 2000 \text{ Jy beam}^{-1}$. The delay tracking center position (0, 0) is $\alpha=05^{\text{h}}35^{\text{m}}14^{\text{s}}.1255$ and $\delta=-05^{\circ}22'36''.475$ (J2000). The LSR velocity of each channel is indicated at the top-right corner of each panel. The synthesized beam pattern is indicated by an ellipse at the bottom left corner of the first panel for the 6.53 km s^{-1} channel. Spot IDs are indicated (see Table 1). Because the spots 2 and 4 are not detected on 2011/137, their positions are obtained from those at the detected epochs (2011/296 and 2011/250 for spots 2 and 4, respectively) by extrapolating their proper motions.

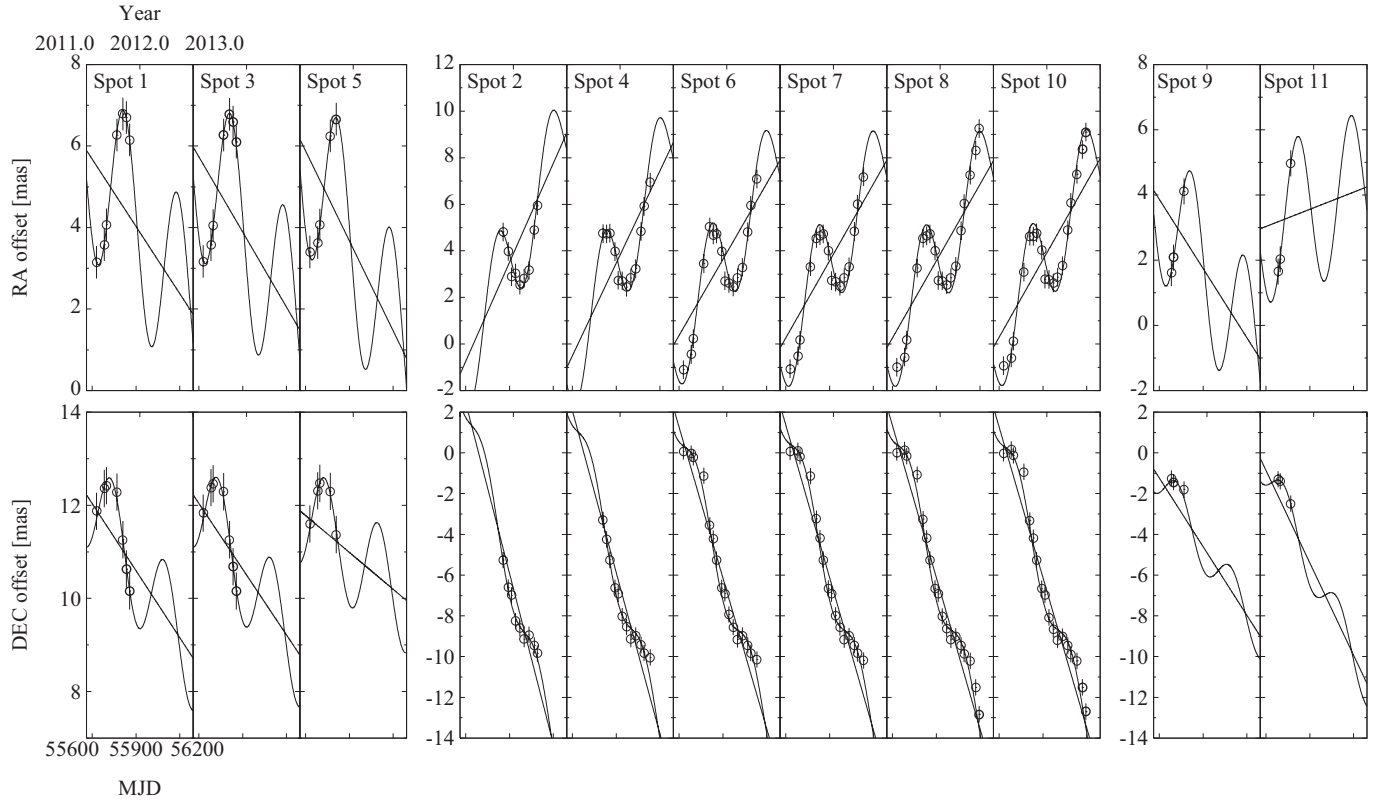


Fig. 7. The position offsets of the supermaser features 1 (spots 1,3,5), 2 (spots 2,4,6,7,8,10) and 3 (spots 9,11) along the right ascension (top panels) and declination (bottom panels) directions as functions of time. A modulation of an annual parallax of 2.39 mas (Kim et al. 2008), as can be seen in the sinusoidal curves, is fixed in the fitting and the proper motion of each spot, as indicated by the straight lines, is fitted (see Table 1). Error bars show typical positional uncertainties estimated from the post-fit residuals, 0.4 mas.

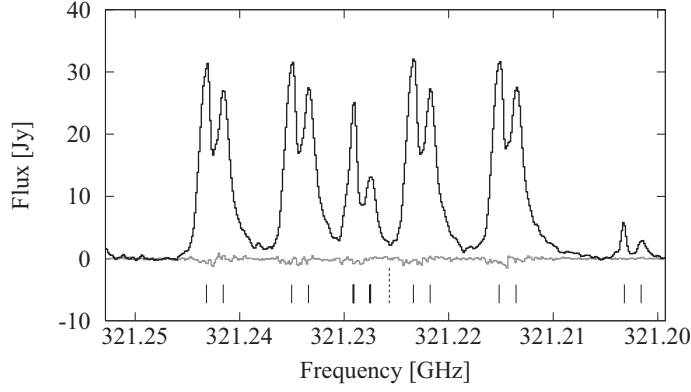


Fig. 8. ALMA band 7 spectra in the Compact Ridge integrated over $2'' \times 2''$ region around the supermaser. Black and grey lines represent spectra using full baselines and those larger than $100 \text{ k}\lambda$, respectively. Frequencies for each line are indicated by solid vertical lines; all show double-peaked structure at 6.9 km s^{-1} and 7.5 km s^{-1} . The transitions and their rest frequencies are $^{13}\text{CH}_3\text{OH}$ ($v_t=0$) $10_{5,6}-11_{4,7}$ at 321.203 GHz , HCOOCH_3 ($v_t=0$) $28_{3,26}-27_{3,25} \text{ E}$ at 321.215 GHz , HCOOCH_3 ($v_t=0$) $28_{3,26}-27_{3,25} \text{ A}$ at 321.223 GHz , HCOOCH_3 ($v_t=1$) $30_{0,30}-29_{1,29} \text{ A}$, $30_{1,30}-29_{0,29} \text{ A}$, $30_{1,30}-29_{1,29} \text{ A}$, and $30_{0,30}-29_{0,29} \text{ A}$ at 321.229 GHz , HCOOCH_3 ($v_t=0$) $28_{2,26}-27_{2,25} \text{ E}$ at 321.235 GHz , and HCOOCH_3 ($v_t=0$) $28_{2,26}-27_{2,25} \text{ A}$ at 321.243 GHz (from high to low velocity; see Splatalogue database). The 7.5 km s^{-1} velocity component for the assumed H_2O ($10_{2,9}-9_{3,6}$) line at 321.226 GHz is indicated by a dashed vertical line.

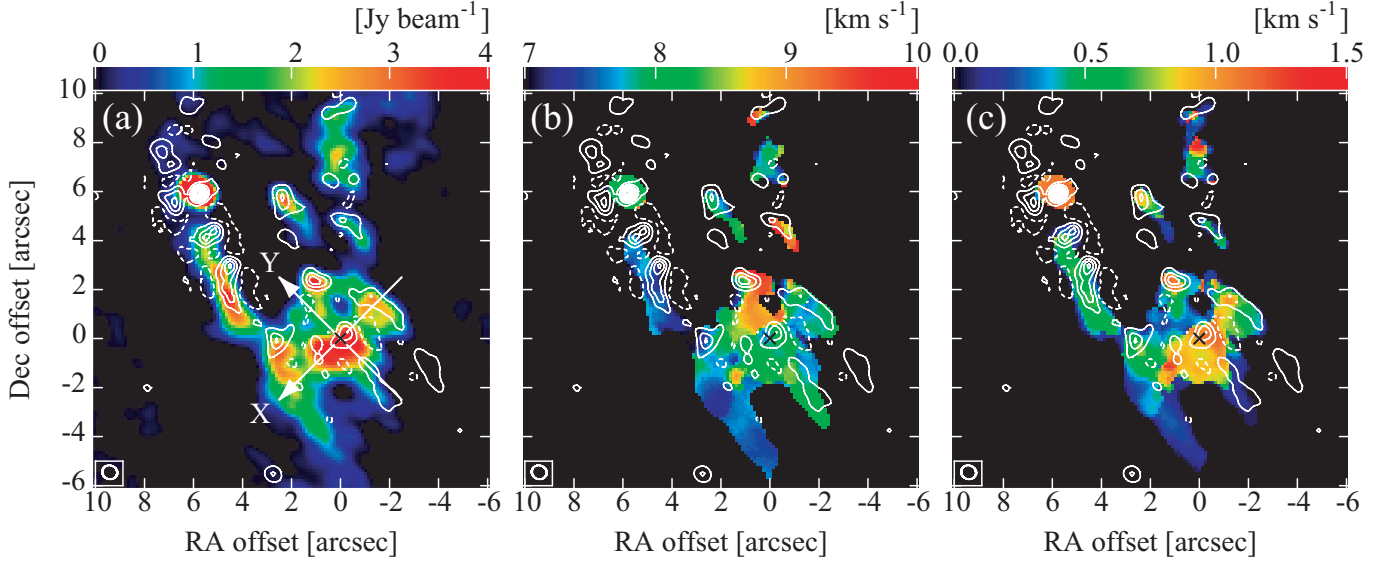


Fig. 9. Continuum map at ALMA band 7 (contour) superposed on moment maps of the HCOOCH_3 line at 321.223 GHz (color). Panels (a), (b), and (c) show the moment 0, 1, and 2 of the HCOOCH_3 line, respectively. The continuum map is obtained with the UV coverage larger than $100 \text{ k}\lambda$ (Hirota et al. 2014b). The interval of contours and the lowest levels are 10σ and $\pm 5\sigma$, respectively, with the rms noise level, σ , of 5 mJy beam^{-1} . A black cross at the $(0,0)$ position in each panel shows the position of the supermaser (e.g. Figure 6). Arrows in panel (a) indicate the X and Y axes employed in the position-velocity maps (Figure 10). The synthesized beam pattern is indicated by a white ellipse at the bottom left corner of each panel.

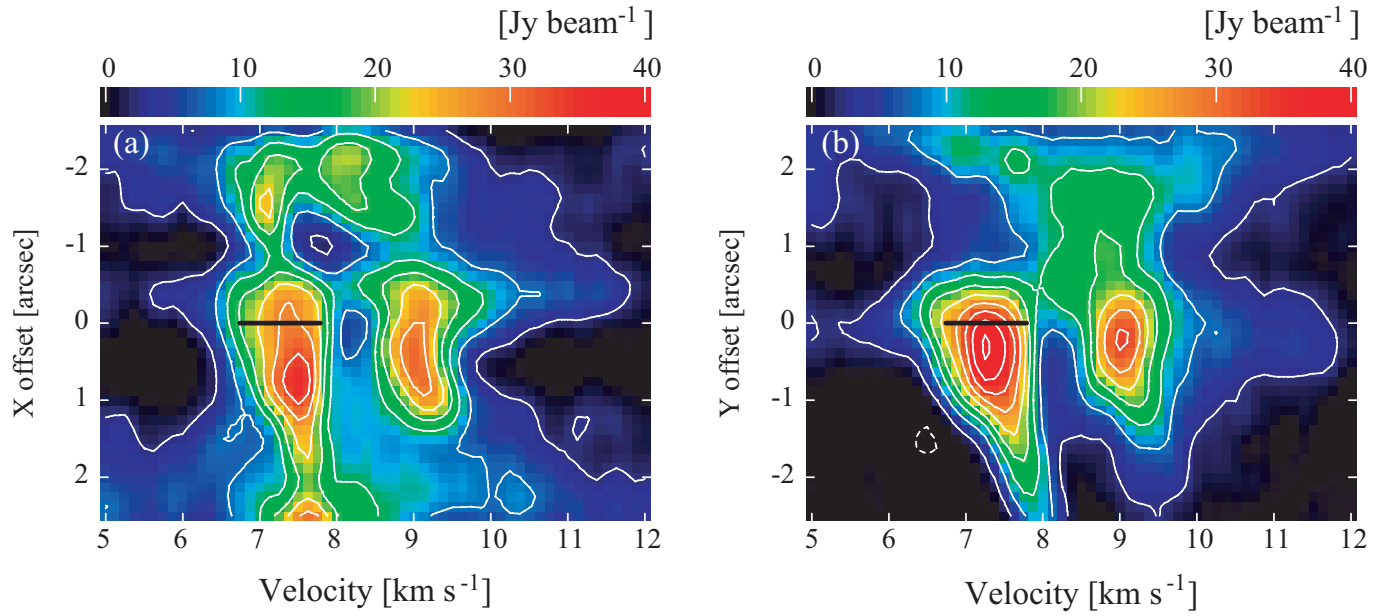


Fig. 10. Position-velocity maps of the HCOOCH₃ line at 321.223 GHz along the (a) X and (b) Y axes. The (0,0) position corresponds to that of the supermaser. Direction of X and Y axes are indicated in Figure 9(a). The interval of contours and the lowest levels are 10σ and $\pm 5\sigma$, respectively, with the rms noise level, σ , of 0.5 Jy beam^{-1} . Positions and velocity ranges of the bursting H₂O maser feature identified in Figure 6, $6.74\text{--}7.79 \text{ km s}^{-1}$, is indicated by a black horizontal bar in each panel.

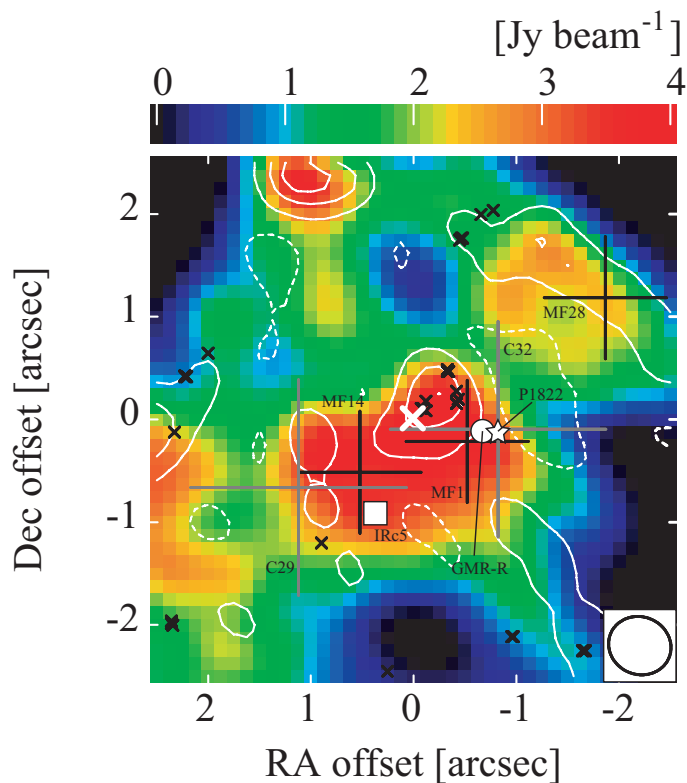


Fig. 11. Zoom-up of the moment 0 map of the HCOOCH_3 line at 321.223 GHz (color) and ALMA band 7 continuum map (contour) around the supermaser (see Figure 9(a)). The (0,0) position corresponds to that of the supermaser. White cross, square, circle, and star represent the positions of the supermaser, infrared source IRc5, radio source GMR-R (Felli et al. 1993), and optical source Parenago 1822, respectively. Positions of the HCOOCH_3 peaks, MF1, 14, and 28 (Favre et al. 2011), and 3 mm continuum peaks, C29 and 32 (Friedel & Weaver 2011), are indicated by black and grey plus signs, respectively, of which sizes correspond to those of the synthesized beams. Black crosses represent positions of the 22 GHz H_2O masers detected by VLA (Gaume et al. 1998). The synthesized beam pattern of the ALMA image is indicated at the bottom right corner.